Nanoscale

PAPER

View Article Online
View Journal | View Issue

Cite this: *Nanoscale*, 2017, **9**, 562

Topological insulating states in 2D transition metal dichalcogenides induced by defects and strain†

Xiaoyin Li,[a,b,c] Shunhong Zhang[a] and Qian Wang*[a,b,c]

Received 6th October 2016,
Accepted 30th November 2016

DOI: 10.1039/c6nr07851f

www.rsc.org/nanoscale

First-principles calculations and extensive analyses reveal that the H phase of two-dimensional (2D) transition metal dichalcogenides (TMDs) can be tuned to topological insulators by introducing square–octagon (4–8) defects and by applying equi-biaxial tensile strain simultaneously. The 2D structure composed of hexagonal rings with 4–8 defects, named sho-TMD, is dynamically and thermally stable. The critical equi-biaxial tensile strain for the topological phase transition is 4%, 6%, and 4% for sho-MoS_2, sho-$MoSe_2$ and sho-WS_2, respectively, and the corresponding nontrivial band gap induced by the spin–orbit coupling is 2, 8, and 22 meV, implying the possibility of observing the helical conducting edge states that are free of backscattering in experiment. It is equally interesting that the size of the energy band gap of the H-phase can be flexibly tuned by changing the concentration of 4–8 defects while the feature of the quasi-direct band gap semiconductor remains. These findings add additional traits to the TMD family, and provide a new strategy for engineering the electronic structure and the band topology of 2D TMDs for applications in nanoelectronics and spintronics.

Two-dimensional (2D) topological insulators (TIs), also called quantum spin Hall insulators, characterized by their insulating bulk and gapless edge states,[1] have attracted considerable attention in recent years because of their fundamental scientific importance and potential applications in electronics and spintronics.[2,3] The edge states of TIs are topologically protected from backscattering of nonmagnetic defects or impurities due to time reversal symmetry, indicating their potential applications in novel quantum devices with low energy dissipation.[4–6] The concept of the quantum spin Hall effect was first proposed in graphene in 2005,[7] since then TI has been a hotly pursued subject of research in condensed matter physics. However, the nontrivial gap in graphene introduced by the rather weak second-order effective spin–orbit coupling (SOC) is small ($\sim 10^{-3}$ meV),[8] which makes the quantum spin Hall state only appear at an unrealistically low temperature. Although the quantum spin Hall effect was experimentally observed in a HgTe quantum well, the operating temperature is still quite low (1.8 K).[6] Therefore, searching for new 2D TIs and tuning the existing 2D semiconducting materials to TIs are of great interest.[9–13]

Atomically thin 2D materials have been extensively investigated since the successful fabrication of graphene in 2004.[14] Among them, the molybdenum disulfide (MoS_2) monolayer, one of transition metal dichalcogenides (TMDs), is of particular interest due to its extraordinary semiconducting characteristics and potential applications in catalysis,[15] lithium ion batteries (LIBs),[16] electronic devices,[17,18] optoelectronics[19,20] and valleytronics.[21] Theoretical studies demonstrated that the MoS_2 monolayer in the 1T′ phase (1T′-MoS_2),[22] the H′ phase (H′-MoS_2)[23] and the T″ phase (T″-MoS_2)[24] exhibits intrinsic topological states with electric field/strain tunable nontrivial band gaps, enriching their potential applications in spintronics. However, the structural distortion in these phases makes them energetically high-lying, thus increasing the difficulty of fabricating these materials. The monolayer MoS_2 with the hexagonal lattice, labeled as H-MoS_2, is the ground state phase in the 2D MoS_2 family with a band gap of 2.13 eV.[25] It is highly desirable to explore the possibility of converting the H-MoS_2 phase from a semiconductor into a TI by modulating its electronic structure. Although a semiconductor-to-TI transition induced by applying an external electric field in phosphorene was theoretically predicted recently,[26] it might be more challenging to tune H-MoS_2 to a TI with an electric field because H-MoS_2 has a larger band gap (2.13 eV)[25] compared to phosphorene (1.5 eV).[26] Moreover, it was reported that it is unlikely to achieve the topological phase transition in H-MoS_2 by applying external strain either.[27] Herein, we propose a new approach

[a]*Center for Applied Physics and Technology, College of Engineering, Peking University; Key Laboratory of High Energy Density Physics Simulation, Ministry of Education, Beijing 100871, China. E-mail: qianwang2@pku.edu.cn*
[b]*Department of Materials Science and Engineering, College of Engineering, Peking University, Beijing 100871, China*
[c]*Collaborative Innovation Center of IFSA (CICIFSA), Shanghai Jiao Tong University, Shanghai 200240, China*

†Electronic supplementary information (ESI) available. See DOI: 10.1039/c6nr07851f

to realize the semiconductor-to-TI transition in H-MoS_2 by tuning the electronic structure of H-MoS_2 using a synergistic effect of defects and strain.

Defects in TMDs, such as point defects,[28,29] dislocations and grain boundaries,[30–32] have been widely studied due to their significant influence on the chemical, mechanical, electronic and optical properties of materials. Our idea is based on the experimental observation and theoretical calculation that 4–8 defects can significantly affect the optical and transport properties of H-MoS_2,[33,34] and the theoretical predications that a 2D MoS_2 composed of square–octagon rings (so-MoS_2)[35] possesses intrinsic topological states with a nontrivial band gap of 13.38 meV.[36,37] We propose a new allotrope of monolayer MoS_2 that is constructed by introducing the 4–8 membered rings as defects into the H-MoS_2 phase, and name it sho-MoS_2. Using state-of-the-art theoretical calculations, we show that sho-MoS_2 is not only dynamically and thermally stable, but also a topological phase transition can be induced by applying equi-biaxial tensile strain. In addition, we explored the topological phase transition of other 2D TMDs including $MoSe_2$, $MoTe_2$, WS_2, WSe_2 and WTe_2 by introducing such defects and strain in their H phases, respectively. Furthermore, we extend this study to the new TMD phases constructed by altering the proportion of 4–8 rings in the sho-structures, and investigate the effect of defects concentration on the electronic properties. Our study suggests that applying equi-biaxial tensile strain plays an important role in engineering the electronic structure and tuning the transport properties of defective TMDs.

First principles calculations and *ab initio* molecular dynamics (AIMD) simulations based on density functional theory (DFT) are carried out using the Vienna *ab initio* simulation package (VASP).[38] A vacuum space of 20 Å in the direction perpendicular to the monolayer sheet of MX_2, where M = (Mo, W) and X = (S, Se, and Te), is used to separate it from its periodic images. Wave functions are expanded using the projector augmented wave (PAW) method[39] with a kinetic energy cutoff of 400 eV. The exchange–correlation potential is incorporated by using the generalized gradient approximation (GGA). In most of our calculations the Perdew–Burke–Ernzerhof (PBE)[40] functional is used whereas for high accuracy electronic structure calculations the hybrid Heyd–Scuseria–Ernzerhof (HSE06)[41,42] functional is adopted. The first Brillouin zone is represented by K points in the reciprocal space sampled using the Monkhorst–Pack scheme[43] with a grid density of $2\pi \times 0.02$ Å^{-1}. The structures are relaxed without any symmetry constraints. The criteria of convergence for energy and atomic force are set to be 10^{-5} eV and 1 meV Å^{-1}, respectively. Tests are also performed using a higher energy convergence criterion of 10^{-8} eV and a denser *k*-grid density of $2\pi \times 0.01$ Å^{-1} to confirm the accuracy of the SOC electronic band structure calculation. The temperature control for NVT-AIMD simulation and NpT-AIMD simulation is achieved by using the Nosé thermostat[44] and Langevin thermostat[45,46] respectively, and the convergence criterion of total energy is set as 1 meV. Phonon calculations are performed by using the finite displacement method implemented in the Phonopy package.[47] The maximally localized Wannier functions (MLWFs) are calculated by using the Wannier90 package[48] interfaced with the Quantum ESPRESSO code.[49]

Fig. 1a shows the optimized atomic structure of sho-MoS_2. Each unit cell contains six Mo and twelve S atoms. The calculated lattice parameters are listed in Table 1. Similar to the other phases of 2D MoS_2,[21–24,28–30] the sho-MoS_2 sheet is composed of three atomic layers with Mo atoms in-between the two layers of S atoms. The Mo–S bond lengths are in the range of 2.40–2.45 Å, close to that in H-MoS_2 (2.42 Å). Analogous to the T′- and so-MoS_2 structures, there exist Mo–Mo bonds in sho-MoS_2, which is absent in the H-MoS_2 structure. The Mo–Mo bond length is 2.67 Å, slightly shorter than that in T′-MoS_2 (2.77 Å). The sho-MoS_2 sheet possesses a rectangular Bravais lattice with D_{2h} symmetry (layer group no. 41, *Pmma*) featured by the coexistence of the four-, six- and eight-membered rings in its geometrical structure. The inversion symmetry exists in this configuration and the reciprocal space has *P*2*mm* symmetry, with four time-reversal-invariant momenta (TRIM) in the irreducible Brillouin zone, namely Γ, M, X, and Y (see Fig. 1b). To study the thermodynamic stability of sho-MoS_2, total energy calculations are performed. The results are given in Table 1, which shows that sho-MoS_2 is energetically metastable compared to H-MoS_2, but it is more stable than some previously reported 2D MoS_2 allotropes such as so-MoS_2, 1T-MoS_2 and H′-MoS_2. The optimized structures of H′-, so-, 1T-, 1T′-, T″- and H-MoS_2 are plotted in Fig. S1 (ESI†). Our calculated results are in excellent agreement with those of previous studies.[22–25,35–37]

To explore the lattice dynamics of sho-MoS_2, the phonon dispersion is calculated, and the results are plotted in Fig. 1c.

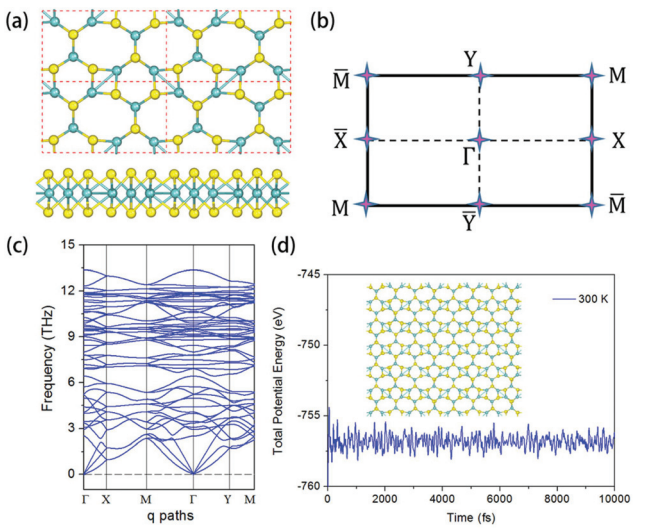

Fig. 1 (a) Optimized structure of sho-MoS_2 from the top and side views. Cyan and yellow spheres represent Mo and S atoms, respectively. (b) First Brillouin zone and high symmetry points (TRIM). (c) Phonon band structure of sho-MoS_2. (d) Evolution of the total potential energy of sho-MoS_2 during the MD simulation. The inset is a snapshot of the structure at the end of the simulation at 300 K.

Table 1 Optimized lattice parameters (in Å), relative energy (E, in eV f.u.$^{-1}$) with respect to H-MoS_2, and the energy band gap (E_g, in eV) calculated using the HSE06 functional without SOC for sho-MoS_2 and some other 2D MoS_2 allotropes

	a	b	E	E_g
sho-MoS_2	9.98	5.70	0.60	0.61
H-MoS_2	3.19	3.19	0	2.13 (ref. 25)
so-MoS_2	6.38	6.38	0.86	0.00 (ref. 36)
1T-MoS_2	3.19	3.19	0.84	0.00 (ref. 25)
1T′-MoS_2	5.72	3.17	0.55	0.00 (ref. 22)
H′-MoS_2	8.80	8.80	0.90	0.00 (ref. 23)
T″-MoS_2	11.23	3.16	0.48	0.42 (ref. 24)
sh^2o-MoS_2	16.40	5.60	0.37	0.45
sh^3o-MoS_2	22.80	5.56	0.27	0.69
sh^4o-MoS_2	29.18	5.55	0.21	0.89

The absence of imaginary modes in the entire Brillouin zone confirms that sho-MoS_2 is dynamically stable. To examine the thermal stability of sho-MoS_2 at room temperature, NVT-AIMD simulation at 300 K is carried out for 10 ps with a time step of 1 fs. To reduce the constraint of periodic boundary conditions, a large supercell of 2 × 4 containing 144 atoms is used for the MD simulation. The results are presented in Fig. 1d, which show that the average value of the total potential energy remains nearly constant, and the 2D sheet maintains its integrated structure without obvious structural distortions during the MD simulation, indicating that sho-MoS_2 is thermally stable at room temperature. Since the initial structure used in the NVT-AIMD simulation is the equilibrium structure at 0 K, considering the influence of temperature on the lattice parameters of the structure, we perform the NpT-AIMD simulation at 300 K as well to obtain more accurate lattice constants. The calculated results (see the ESI, Fig. S2†) show that the average value of lattice parameters of the 2D sheet during the 300 K NpT-AIMD simulation is nearly the same as that of the equilibrium structure at 0 K, which confirms our results of NVT-AIMD simulation.

In order to study the electron delocalization behavior of sho-MoS_2, we calculate its electron localization function (ELF), which is based on the jellium electron gas model and its value is renormalized between 0.0 and 1.0. The values of 0.5 and 1.0 represent fully delocalized (homogeneous electron gas) and fully localized electrons, respectively, while the value of 0.0 refers to a very low charge density. From the ELF slices shown in Fig. 2a and b, we note that the electrons are more localized around the S atoms in the S layer, while in the Mo layer the delocalized electrons are distributed in the space between the Mo atoms. However, the Mo sites have low electron density, and no fully localized electrons are observed neither in the Mo nor in the S layer.

We then calculate the electronic band structure and the projected density of states (PDOS) of sho-MoS_2 to study its electronic properties. The results are plotted in Fig. 2c, which show that sho-MoS_2 is a direct band gap semiconductor with a band gap of 0.35 eV at the PBE level. Considering the well-known underestimation of PBE functional in predicting the electronic band gap, we use the hybrid HSE06 functional to reach a more accurate result, which yields the band gap of 0.61 eV (Fig. 2c). Comparing with the band gap of 2.13 eV for H-MoS_2,[25] there is an obvious reduction in sho-MoS_2, indicating that the electronic band structure of H-MoS_2 can be effectively tuned by altering the atomic configuration. A detailed analysis of the orbital-projected DOS (Fig. 2c) reveals that the electronic states near the Fermi level primarily originate from the Mo-4d and S-3p orbitals, which is confirmed by calculating its MLWFs (see the ESI, Fig. S3†).

Having obtained the band structure and identified the orbital composition of the frontier bands, we explore the possibility of engineering the electronic band structure and band topology of sho-MoS_2 by applying equi-biaxial tensile strain, which has been demonstrated to be an effective way to tune the electronic structure of low dimensional materials.[50,51] The band structure (along the X–Γ–Y path) evolution with different magnitudes of equi-biaxial tensile strain is given in Fig. S4

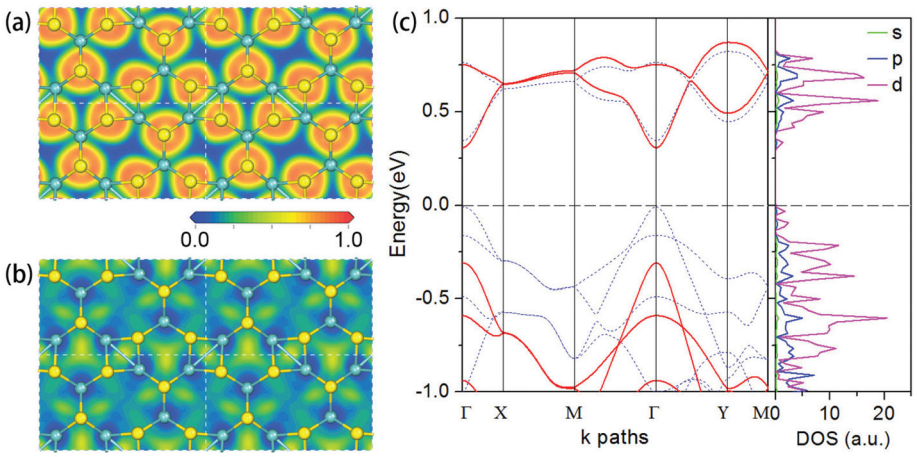

Fig. 2 Slice form of electron localization function crossing (a) the S layer, (b) the Mo layer, and (c) electronic band structure and orbital projected DOS of sho-MoS_2. Blue dashed lines and red solid lines in the band structure correspond to the PBE and HSE06 results, respectively.

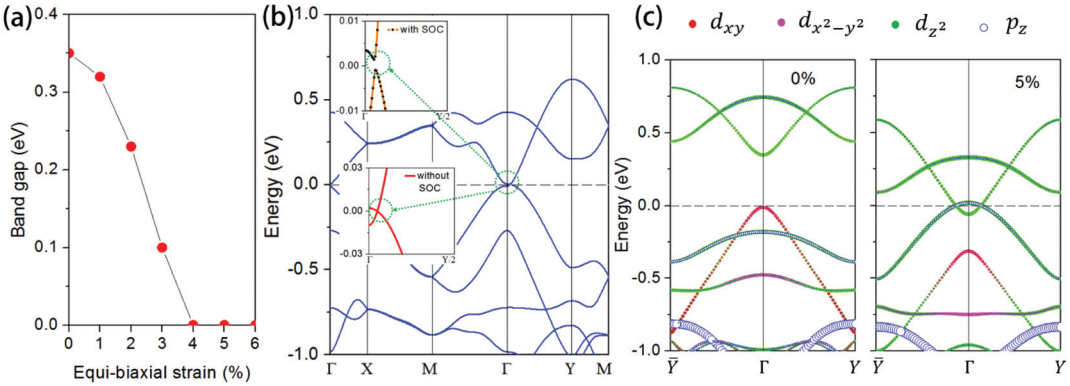

Fig. 3 (a) Band gap of sho-MoS_2 as a function of equi-biaxial tensile strain calculated at the PBE level. (b) Electronic band structure of sho-MoS_2 along the high symmetry path in the first Brillouin zone with 4% equi-biaxial tensile strain. The insets are the zoomed in band structure near the Γ point with and without SOC interaction. (c) Orbital-decomposed band structure without SOC for sho-MoS_2 with an equilibrium lattice and under 5% strain, respectively.

(ESI†), and the band gap as a function of the strain is plotted in Fig. 3a, which shows that the band gap decreases with increasing tensile strain, and is finally closed when the applied tensile strain reaches 4%, showing a strain induced semiconductor-to-metal transition.

To study the transition mechanism, we calculate the orbital-decomposed band structure of sho-MoS_2 under different equi-biaxial tensile strain. The results are plotted in Fig. S5 (ESI†). For simplicity, we term the highest occupied band and the lowest unoccupied band as the highest valence band (HVB) and the lowest conduction band (LCB) respectively. We find that the HVB is mainly from the Mo-d_{xy} and Mo-$d_{x^2-y^2}$ orbitals, the second highest occupied band (HVB-1) is mainly contributed by the S-p_z and Mo-d_{z^2} orbitals, while the LCB dominantly comes from the Mo-d_{z^2} orbital. On increasing the strain, the energy of the HVB-1 exceeds that of the HVB at the Γ point forming a new HVB, and finally the new HVB touches the LCB under the strain of 4%, achieving the semiconductor-to-metal transition. We note that such a trend of the band gap decreasing with the increase of tensile strain was also observed in other semiconductors.[52] Generally, when equi-biaxial tensile strain is applied to a structure, the atoms in the crystal are pulled apart and the interatomic interaction decreases, thus the resulting bonding and antibonding energy states become closer in energy, which leads to a decrease of the band gap. Finally the semiconductor-to-metal transition is achieved when the strain is further increased to close the band gap.

The electronic band structure of sho-MoS_2 with 4% equi-biaxial tensile strain is shown in Fig. 3b. One can see that the valence band maximum (VBM) and the conduction band minimum (CBM) inverse at the Γ point. The highest valence band (HVB) and the lowest conduction band (LCB) cross at the point located at the Γ–Y path, forming a Dirac cone (inset of Fig. 3b). Furthermore, the Dirac point locates exactly on the Fermi energy. After turning on the SOC, we observe that a small band gap of 2 meV is opened (inset of Fig. 3b), which is assumed to be topologically nontrivial. To further confirm the topological nontrivial nature, we calculate the Z_2 topological invariant (ν) of sho-MoS_2 under different equi-biaxial tensile strain. Due to the inversion symmetry in the sho-MoS_2 structure, the topological invariant ν can be directly computed based on the parity of the wave function of occupied states at the four time-reversal-invariant momenta.[53,54] We obtain ν by using the equation

$$\delta(K_i) = \prod_{m=1}^{N} \xi_{2m}^{i}, (-1)^{\nu} = \prod_{i=1}^{4} \delta(K_i) = \delta(\Gamma)\delta(\mathrm{X})\delta(\mathrm{Y})\delta(\mathrm{M}).$$

here δ (K_i) represents the product of the parity eigenvalue at different time-reversal-invariant momenta, $\xi_{2m} = \pm 1$ is the parity eigenvalue of the wave function of the $2m$-th occupied energy band at time-reversal-invariant momenta K_i, and N is the total number of degenerate occupied bands. According to the Z_2 classification, $\nu = 1$ characterizes the topologically nontrivial phase, whereas $\nu = 0$ indicates trivial band topology. The calculated Z_2 number of the sho-MoS_2 structure with 3% and 4% equi-biaxial tensile strain is 0 and 1, respectively, suggesting a quantum phase transition from a normal semiconductor to a 2D TI. We then carefully investigate the orbital contributions to the bands near the Fermi level under 0% and 5% tensile strain by comparing their orbital-decomposed band structures. The results are presented in Fig. 3c. As stated above the band order of the HVB and HVB-1 interchanges when the magnitude of the strain exceeds 2%. Further elevating the strain leads to the inversion of the new VBM and the CBM in the vicinity of the Γ point. This inversion of band edges under strain implies a topological phase transition which is analogous to the strain induced topological phase transition in T″-MoS_2.[24] In addition, band structure calculations are also performed using the HSE06 hybrid functional to confirm our finding of quantum phase transition induced by equi-biaxial tensile strain. They reproduce the band gap decrease trend obtained at the PBE level. However, the critical strain for the semiconductor-to-metal transition predicted by the PBE functional is smaller than that of the HSE06 functional, similar to the case with the arsenene sheet.[51] Based on the HSE06 functional,

the critical strain to induce a quantum phase transition in sho-MoS_2 is 6%, which is confirmed by calculating the Z_2 number. Therefore, the strain induced quantum phase transition is an intrinsic property of sho-MoS_2 independent of the choice of the exchange–correlation functional.

Since the SOC is stronger in heavy atoms (approximately proportional to Z^4, here Z represents the atomic number), we expect that the nontrivial band gap can be larger in the sho-$MoSe_2$, $MoTe_2$, WS_2, WSe_2 and WTe_2 monolayers with similar geometrical structures to that of sho-MoS_2. Hence we calculate their electronic band structures. From the results shown in Fig. S6 (ESI†), one can see that sho-$MoTe_2$, sho-WSe_2 and sho-WTe_2 are normal metals while sho-$MoSe_2$ and sho-WS_2 are semiconductors with a direct band gap of 0.10 and 0.20 eV, respectively. The electronic band structures of sho-$MoSe_2$ and sho-WS_2 are analogous to that of sho-MoS_2. Therefore, it is interesting to study whether there exists a strain induced topological phase transition in these compounds. The optimized structures of these two nanosheets are presented in Fig. 4a and c. We first calculate their phonon dispersion to examine their structural stability. The results are presented in Fig. 4b and d. There are no imaginary modes in the entire Brillouin zone for both sho-$MoSe_2$ and sho-WS_2, confirming that both of them are dynamically stable. Then we investigate the evolution of their electronic band structure under different equi-biaxial tensile strains. The band gap as a function of the applied tensile strain for the two structures is plotted in Fig. S6f (ESI†), which shows that there exists a semiconductor-to-metal transition for both of them. The electronic band structure of sho-$MoSe_2$ (sho-WS_2) under different magnitudes of tensile strain is plotted in Fig. S7 (ESI†). In the case of sho-$MoSe_2$, the band gap closes as the strain increases to 6%, while for sho-WS_2 the critical strain for band gap closure is 4%. The electronic band structures with and without the SOC for the 6% (4%) strained sho-$MoSe_2$ (sho-WS_2) sheet are given in Fig. 4e (4f). The inclusion of the SOC opens a band gap of 8 (22) meV for the strained sho-$MoSe_2$ (WS_2). To explore their topological nature, we calculate the topological invariant Z_2 number ν of the two structures under different equi-biaxial tensile strains. The results are listed in Fig. 4g and h, which confirm that the topological phase transition occurs when the tensile strain reaches 6% (4%) for sho-$MoSe_2$ (sho-WS_2). A larger tensile strain (6%) required for the phase transition in sho-$MoSe_2$ (while that for sho-MoS_2 and sho-WS_2 is 4%) may result from a larger tensile strain required for the inversion of HVB-1 and HVB in sho-$MoSe_2$ (~4% for sho-$MoSe_2$, ~1% for sho-MoS_2 and ~2% for sho-WS_2, see the ESI, Fig. S4 and S7†).

The sho-MoS_2 sheet has a direct band gap of 0.61 eV, analogous to that of the recently reported silicon allotrope, h-Si_6,[55] showing its potential applications in photovoltaic and nanoelectronic devices. Wave function analysis of the VBM and CBM at the Γ point confirms that the interband dipole transition between them is symmetrically allowed. In the sho-MoS_2 structure, the point group at the Γ point is D_{2h}, which has eight one-dimensional irreducible representations. It is found that the VBM belongs to B_{1g} representation while the CBM belongs to B_{3u} representation. The dipole moment operator for the dipole transition in the D_{2h} group can be represented as $(B_{1u}\oplus B_{2u}\oplus B_{3u})$. The direct product for the three representations, written as $B_{1g}\otimes(B_{1u}\oplus B_{2u}\oplus B_{3u})\otimes B_{3u}$, can be reduced to $B_{3g}\oplus A_g\oplus B_{1g}$, which contains the full symmetry representation A_g, demonstrating that the diploe transition through the direct

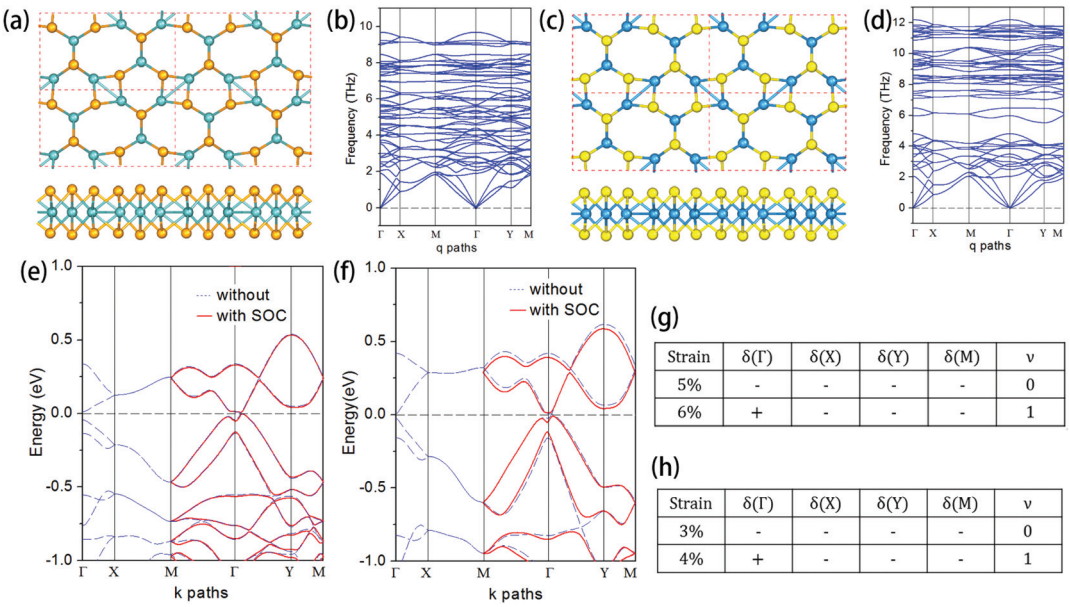

Strain	δ(Γ)	δ(X)	δ(Y)	δ(M)	ν
5%	-	-	-	-	0
6%	+	-	-	-	1

Strain	δ(Γ)	δ(X)	δ(Y)	δ(M)	ν
3%	-	-	-	-	0
4%	+	-	-	-	1

Fig. 4 Optimized structures of (a) sho-$MoSe_2$ and (c) sho-WS_2 from the top and side views. Phonon dispersion along the high symmetry path in the first Brillouin zone of (b) sho-$MoSe_2$ and (d) sho-WS_2. The electronic band structure of (e) sho-$MoSe_2$ with 6% tensile strain, and (f) sho-WS_2 with 4% tensile strain. (g) and (h) are δ at time-reversal-invariant momenta for sho-$MoSe_2$ and sho-WS_2 with different magnitudes of equi-biaxial tensile strain and the corresponding Z_2 invariant, ν, respectively.

band gap at the Γ point is symmetrically allowed. The result shows that photon excitation at the Γ point is free of phonon mediation thus easy to be achieved.

The carrier effective mass m^* for photovoltaic materials is a key factor to determine their performance. Thus, we calculate the effective mass of the band edge electrons and holes of sho-MoS_2 at the Γ point along the x (y) direction. The band edge electron (hole) effective mass can be calculated by a quadratic fitting of the conduction (valence) band along a certain direction in the momentum space

$$\frac{1}{m^*} = \frac{1}{\hbar^2}\frac{\partial^2 E}{\partial k^2}.$$

The results are listed in Table 2 and the calculated carrier effective masses of H-MoS_2 are consistent with previous studies.[56,57] We note that the carrier effective masses of sho-MoS_2 are different along the x and y directions, namely $m_e^*(x) = 1.62m_e^*(y)$, and $m_h^*(x) = 2.80m_h^*(y)$, which shows an anisotropic character. Compared with H-MoS_2, sho-MoS_2 has a larger carrier effective mass along the x direction whereas the carrier effective mass along the y direction is smaller, suggesting that carriers prefer to transport along the y direction in sho-MoS_2. We then explore the influence of strain on the carrier effective mass of sho-MoS_2. The results listed in Table 2 show that the effective masses of electrons and holes at the Γ point can be effectively tuned by applying equi-biaxial tensile strain. As the strain increases, the effective masses of carriers decrease significantly, except in the case of holes along the y direction. The effective mass of holes along the y direction firstly decreases as the strain increases, however a sharp increase occurs as the strain reaches 2%. After this, the effective mass of holes decreases again. The reason for the sharp increase of the hole effective mass is that the energy of HVB-1 exceeds that of HVB at the Γ point when strain reaches up to 2%, as shown in Fig. S4 (ESI†), and the band curvatures of HVB and HVB-1 are different.

Finally, we study the modulation of the electronic structures of the H-phase of TMD with different concentrations of the square–octagonal defects. We take H-MoS_2 as an example. When lowering the concentration of the square–octagonal line defects in H-MoS_2, the structure becomes hexagon-rich. The hexagon-rich MoS_2 structure is termed sh^{n}o-MoS_2, where n refers to the number of hexagons between the two neighboring squares along the crystal axis a, as illustrated in Fig. 5a.

Table 2 Electron and hole effective masses (m^*) at the Γ point along the Γ–X (Γ–Y) direction of sho-MoS_2 in the equilibrium state and under equi-biaxial tensile strain. Electron and hole effective masses at the K point (1/3, 1/3) along the K–Γ (K–M) direction of H-MoS_2, where the fractional reciprocal coordinates for the Γ and M are (0, 0) and (1/2, 0), respectively. The unit is the electron rest mass (m_0)

	H-MoS_2		sho-MoS_2				
m^*/m_0		0%		0%	1%	2%	3%
m_e^*	K(Γ)	0.456	Γ(X)	0.548	0.538	0.492	0.361
	K(M)	0.467	Γ(Y)	0.338	0.310	0.288	0.273
m_h^*	K(Γ)	0.565	Γ(X)	0.866	0.873	0.722	0.432
	K(M)	0.590	Γ(Y)	0.309	0.293	1.885	1.480

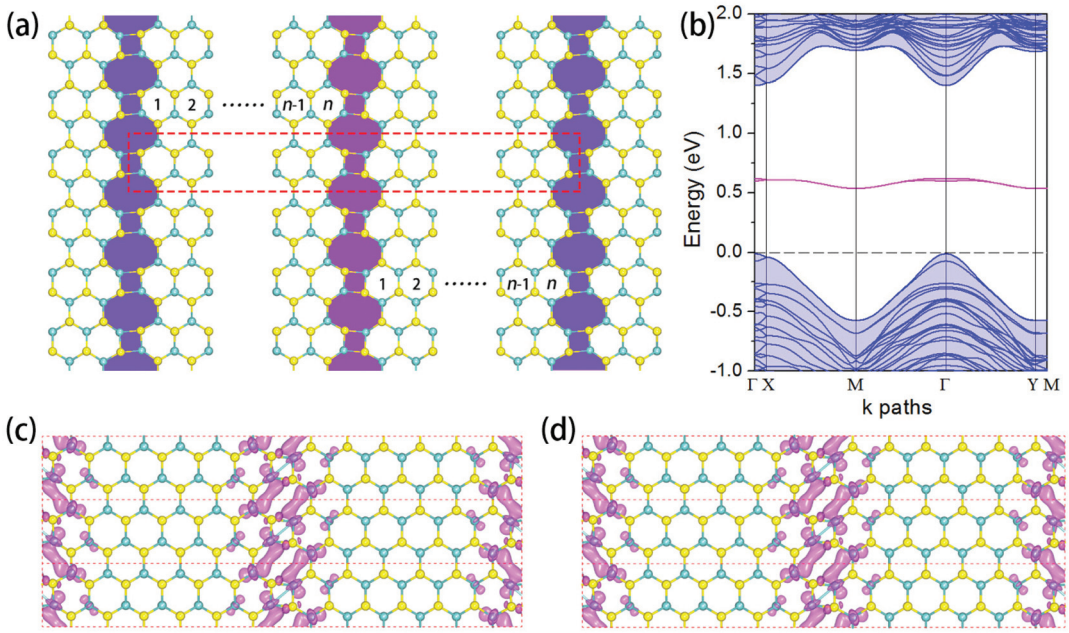

Fig. 5 (a) Schematic illustration of the geometric structure of sh^{n}o-MoS_2. The square and octagonal rings in the line defects are filled in purple and magenta. (b) The electronic band structure for sh^{6}o-MoS_2. The purple lines represent defect states induced by square–octagonal rings. (c) and (d) are the band-decomposed charge density isosurfaces (isovalue: 0.01 e Å^{-3}) for the two lowest unoccupied bands of sh^{6}o-MoS_2. The unit cells are marked by red dashed-line rectangles.

The larger the number of n, the smaller the concentration of the defects in H-MoS_2. The optimized structures of sh^{n}o-MoS_2 (n = 2–6) are presented in Fig. S8 (ESI†). The calculated lattice parameters and relative energies are listed in Table S2 (ESI†). When n increases to 2, the energy of sh^{n}o-MoS_2 becomes lower than all the other known phases of 2D MoS_2 except for the H phase. The calculated band structures of sh^{n}o-MoS_2 (n > 1) are plotted in Fig. S9 (ESI†), where one can see a significant change compared to the sho-structure: the lowest and second lowest unoccupied energy bands become less dispersed as n increases, indicating that the states are highly localized (as evidenced by the total DOS in the ESI,† Fig. S10). The HSE06 band gap results for the sh^{n}o-MoS_2 structures with n = 1–4 are listed in Table 1 and the PBE band gap results for structures with n = 1–6 are listed in Table S2 (ESI†). The square–octagonal rings can be viewed as an artificial line defect in H-MoS_2 and its electronic structure can be modulated *via* controlling the defect concentration, that is the value of n. From the electronic band structure of sh^{6}o-MoS_2 in Fig. 5b, we can see that the two lowest unoccupied bands are nearly flat. Calculations of the band-decomposed charge density show that the two bands originate from the square–octagonal rings, as shown in Fig. 5c and d, which accounts for their dispersionless feature. Because the square–octagonal rings can be viewed as parallelly aligned artificial line defects, the two lowest unoccupied bands can be classified as the defect states. The defect states are located at the mid-position between the valence and conduction bands of pristine H-MoS_2. These mid-gap states induced by incorporating the square–octagonal defects into the H-MoS_2 phase, which is typical in semiconductors,[33] could act as sinks for carriers, thus significantly affecting the optical and transport properties of the materials. When the n value is large enough, the square–octagonal line defects can be viewed as grain boundaries just like the case of 4–8 grain boundaries in the previous study.[34] As n decreases, the defect concentration increases and the interaction between the neighboring line defects becomes stronger, consequently the defect states become more and more delocalized (see the ESI, Fig. S11†), thus effectively tuning the electronic structure of sh^{n}o-MoS_2.

In summary, using density functional theory based first principles calculations, we studied the defects and strain induced topological phase transition in H-phase TMDs. We proposed a family of monolayer TMD structures by introducing the experimentally observed 4–8 defects into the H phase of 2D TMDs, named sho-TMDs. Compared to the ground state H-MoS_2 phase, sho-MoS_2 is energetically metastable, but it is thermodynamically more stable than the previously reported H′-phase, so-phase and 1T-phase, and is thermally stable at room temperature. The predicted sho-MoS_2 structure has a direct band gap of 0.61 eV at the Γ point, which decreases monotonously when an equi-biaxial tensile strain is applied to the structure. We identified a topological phase transition when the strain reaches 4%. Calculations of the topological invariant Z_2 number suggest that the strained sho-MoS_2 becomes a topological insulator, and the SOC induced nontrivial band gap is 2 meV. Such quantum phase transition is also predicted in the structurally analogous sho-$MoSe_2$ and sho-WS_2 sheets, which display larger nontrivial band gaps of 8 and 22 meV, respectively. The larger nontrivial band gap in sho-WS_2 is more probable for experimental observations. The band edge carrier effective mass of sho-MoS_2 exhibits significant anisotropy. Compared with that of H-MoS_2, the carrier effective mass of sho-MoS_2 is lighter along the y direction, and can be tailored *via* external strain. We found that incorporating less 4–8 motifs into the H-TMD structure enhances the thermodynamic stability and significantly changes the band structure, which provides a new degree of freedom to engineer the electronic structures of 2D TMDs. When the n value in sh^{n}o-MoS_2 reaches 2, the structure is energetically more stable than all the other known phases of 2D MoS_2 except for the H phase. Further increase of n value makes the mid-gap states induced by 4–8 defects become more localized. These states could act as traps for carriers, and would significantly affect the optical and transport properties of the materials. In fact, defects widely exist in materials, studying the effect of defects on properties is of significance in practice. We believe that our theoretical study would stimulate more experimental efforts on the exploration of defect-induced quantum spin Hall insulating states in 2D TMD materials.

Acknowledgements

This work is partially supported by grants from the National Natural Science Foundation of China (NSFC-51471004), the National Grand Fundamental Research 973 Program of China (Grant 2012CB921404), and the Doctoral Program of Higher Education of China (20130001110033). The authors would like to thank Dr Jian Zhou (Department of Physics, Virginia Commonwealth University) for stimulating discussions. The calculations were carried out at the National Supercomputer Center in Guangzhou (Tianhe-II).

References

1 M. Z. Hasan and C. L. Kane, *Rev. Mod. Phys.*, 2010, **82**, 3045–3067.
2 E. O. Wrasse and T. M. Schmidt, *Nano Lett.*, 2014, **14**, 5717–5720.
3 A. Wang, X. Zhang and M. Zhao, *Nanoscale*, 2014, **6**, 11157–11162.
4 N. Nagaosa, *Science*, 2007, **318**, 758–759.
5 B. A. Bernevig, T. L. Hughes and S.-C. Zhang, *Science*, 2006, **314**, 1757–1761.
6 M. König, S. Wiedmann, C. Brüne, A. Roth, H. Buhmann, L. W. Molenkamp, X.-L. Qi and S.-C. Zhang, *Science*, 2007, **318**, 766–770.
7 C. L. Kane and E. J. Mele, *Phys. Rev. Lett.*, 2005, **95**, 226801.
8 Y. Yao, F. Ye, X.-L. Qi, S.-C. Zhang and Z. Fang, *Phys. Rev. B: Condens. Matter*, 2007, **75**, 041401.

9 Y. Ma, Y. Dai, L. Kou, T. Frauenheim and T. Heine, *Nano Lett.*, 2015, **15**, 1083–1089.
10 C. P. Crisostomo, L.-Z. Yao, Z.-Q. Huang, C.-H. Hsu, F.-C. Chuang, H. Lin, M. A. Albao and A. Bansil, *Nano Lett.*, 2015, **15**, 6568–6574.
11 J. Hu, J. Alicea, R. Wu and M. Franz, *Phys. Rev. Lett.*, 2012, **109**, 266801.
12 L. Chen, Z. F. Wang and F. Liu, *Phys. Rev. B: Condens. Matter*, 2013, **87**, 235420.
13 Y. Li, P. Tang, P. Chen, J. Wu, B.-L. Gu, Y. Fang, S. B. Zhang and W. Duan, *Phys. Rev. B: Condens. Matter*, 2013, **87**, 245127.
14 K. S. Novoselov, A. K. Geim, S. V. Morozov, D. Jiang, Y. Zhang, S. V. Dubonos, I. V. Grigorieva and A. A. Firsov, *Science*, 2004, **306**, 666–669.
15 A. B. Laursen, S. Kegnaes, S. Dahl and I. Chorkendorff, *Energy Environ. Sci.*, 2012, **5**, 5577–5591.
16 H. Hwang, H. Kim and J. Cho, *Nano Lett.*, 2011, **11**, 4826–4830.
17 S. Bertolazzi, J. Brivio and A. Kis, *ACS Nano*, 2011, **5**, 9703–9709.
18 D. Akinwande, N. Petrone and J. Hone, *Nat. Commun.*, 2014, **5**, 5678.
19 A. Kumar and P. K. Ahluwalia, *Eur. Phys. J. B*, 2012, **85**, 186.
20 O. Lopez-Sanchez, D. Lembke, M. Kayci, A. Radenovic and A. Kis, *Nat. Nanotechnol.*, 2013, **8**, 497–501.
21 T. Cao, G. Wang, W. Han, H. Ye, C. Zhu, J. Shi, Q. Niu, P. Tan, E. Wang, B. Liu and J. Feng, *Nat. Commun.*, 2012, **3**, 887.
22 X. Qian, J. Liu, L. Fu and J. Li, *Science*, 2014, **346**, 1344–1347.
23 Y. Ma, L. Kou, X. Li, Y. Dai and T. Heine, *Phys. Rev. B: Condens. Matter*, 2016, **93**, 035442.
24 F. Ma, G. Gao, Y. Jiao, Y. Gu, A. Bilic, H. Zhang, Z. Chen and A. Du, *Nanoscale*, 2016, **8**, 4969–4975.
25 M. Kan, J. Y. Wang, X. W. Li, S. H. Zhang, Y. W. Li, Y. Kawazoe, Q. Sun and P. Jena, *J. Phys. Chem. C*, 2014, **118**, 1515–1522.
26 Q. Liu, X. Zhang, L. B. Abdalla, A. Fazzio and A. Zunger, *Nano Lett.*, 2015, **15**, 1222–1228.
27 H. Shi, H. Pan, Y.-W. Zhang and B. I. Yakobson, *Phys. Rev. B: Condens. Matter*, 2013, **87**, 155304.
28 W. Zhou, X. Zou, S. Najmaei, Z. Liu, Y. Shi, J. Kong, J. Lou, P. M. Ajayan, B. I. Yakobson and J.-C. Idrobo, *Nano Lett.*, 2013, **13**, 2615–2622.
29 H. Liu, N. Han and J. Zhao, *RSC Adv.*, 2015, **5**, 17572–17581.
30 Y. Han, T. Hu, R. Li, J. Zhou and J. Dong, *Phys. Chem. Chem. Phys.*, 2015, **17**, 3813–3819.
31 S. Zhou and J. Zhao, *J. Phys. Chem. C*, 2016, **120**, 21691–21698.
32 S. Wang, G.-D. Lee, S. Lee, E. Yoon and J. H. Warner, *ACS Nano*, 2016, **10**, 5419–5430.
33 A. M. van der Zande, P. Y. Huang, D. A. Chenet, T. C. Berkelbach, Y. You, G.-H. Lee, T. F. Heinz, D. R. Reichman, D. A. Muller and J. C. Hone, *Nat. Mater.*, 2013, **12**, 554–561.
34 X. Zou, Y. Liu and B. I. Yakobson, *Nano Lett.*, 2013, **13**, 253–258.
35 W. Li, M. Guo, G. Zhang and Y.-W. Zhang, *Phys. Rev. B: Condens. Matter*, 2014, **89**, 205402.
36 S. M. Nie, Z. Song, H. Weng and Z. Fang, *Phys. Rev. B: Condens. Matter*, 2015, **91**, 235434.
37 Y. Ma, L. Kou, X. Li, Y. Dai, S. C. Smith and T. Heine, *Phys. Rev. B: Condens. Matter*, 2015, **92**, 085427.
38 G. Kresse and J. Furthmuller, *Phys. Rev. B: Condens. Matter*, 1996, **54**, 11169–11186.
39 P. E. Blöchl, *Phys. Rev. B: Condens. Matter*, 1994, **50**, 17953–17979.
40 J. P. Perdew, K. Burke and M. Ernzerhof, *Phys. Rev. Lett.*, 1996, **77**, 3865–3868.
41 J. Heyd, G. E. Scuseria and M. Ernzerhof, *J. Chem. Phys.*, 2003, **118**, 8207–8215.
42 J. Heyd, G. E. Scuseria and M. Ernzerhof, *J. Chem. Phys.*, 2006, **124**, 219906.
43 H. J. Monkhorst and J. D. Pack, *Phys. Rev. B: Solid State*, 1976, **13**, 5188–5192.
44 S. Nose, *J. Chem. Phys.*, 1984, **81**, 511–519.
45 M. Parrinello and A. Rahman, *Phys. Rev. Lett.*, 1980, **45**, 1196–1199.
46 M. Parrinello and A. Rahman, *J. Appl. Phys.*, 1981, **52**, 7182–7190.
47 A. Togo, F. Oba and I. Tanaka, *Phys. Rev. B: Condens. Matter*, 2008, **78**, 134106.
48 A. A. Mostofi, J. R. Yates, Y. S. Lee, I. Souza, D. Vanderbilt and N. Marzari, *Comput. Phys. Commun.*, 2008, **178**, 685–699.
49 G. Paolo, B. Stefano, B. Nicola, C. Matteo, C. Roberto, C. Carlo, C. Davide, L. C. Guido, C. Matteo, D. Ismaila, C. Andrea Dal, G. Stefano de, F. Stefano, F. Guido, G. Ralph, G. Uwe, G. Christos, K. Anton, L. Michele, M.-S. Layla, M. Nicola, M. Francesco, M. Riccardo, P. Stefano, P. Alfredo, P. Lorenzo, S. Carlo, S. Sandro, S. Gabriele, P. S. Ari, S. Alexander, U. Paolo and M. W. Renata, *J. Phys.: Condens. Matter*, 2009, **21**, 395502.
50 J. Zhou, Q. Wang, Q. Sun and P. Jena, *Nano Res.*, 2016, **9**, 1578–1589.
51 H. Zhang, Y. Ma and Z. Chen, *Nanoscale*, 2015, **7**, 19152–19159.
52 Q. Yan, P. Rinke, A. Janotti, M. Scheffler and C. G. Van de Walle, *Phys. Rev. B: Condens. Matter*, 2014, **90**, 125118.
53 W. Feng, J. Wen, J. Zhou, D. Xiao and Y. Yao, *Comput. Phys. Commun.*, 2012, **183**, 1849–1859.
54 L. Fu and C. L. Kane, *Phys. Rev. B: Condens. Matter*, 2006, **74**, 195312.
55 Y. Guo, Q. Wang, Y. Kawazoe and P. Jena, *Sci. Rep.*, 2015, **5**, 14342.
56 Y. Cai, G. Zhang and Y.-W. Zhang, *J. Am. Chem. Soc.*, 2014, **136**, 6269–6275.
57 W. S. Yun, S. W. Han, S. C. Hong, I. G. Kim and J. D. Lee, *Phys. Rev. B: Condens. Matter*, 2012, **85**, 033305.

Supplementary Information for

Topological insulating states in 2D transition metal dichalcogenides induced by defects and strain

Xiaoyin Li,[a, b, c] Shunhong Zhang,[a] and Qian Wang*[a, b, c]

[a] Center for Applied Physics and Technology, College of Engineering, Peking University; Key Laboratory of High Energy Density Physics Simulation, Ministry of Education, Beijing 100871, China.

[b] Department of Materials Science and Engineering, College of Engineering, Peking University, Beijing 100871, China.

[c] Collaborative Innovation Center of IFSA (CICIFSA), Shanghai Jiao Tong University, Shanghai 200240, China.

Contents

Supplementary Figures

Figure S1. Optimized structures of 2D MoS_2 polymorphs.

Figure S2. NpT-AIMD simulation results of sho-MoS_2.

Figure S3. MLWFs of sho-MoS_2.

Figure S4. Band structure evolution of sho-MoS_2 under equi-biaxial tensile strain.

Figure S5. Orbital projected band structure of sho-MoS_2 under equi-biaxial tensile strain.

Figure S6. Band structure of sho-TMD, and band gap of sho-$MoSe_2$ and sho-WS_2 under strain.

Figure S7. Band structure evolution of sho-$MoSe_2$ and sho-WS_2 under equi-biaxial tensile strain.

Figure S8. Optimized structures of sh^{n}o-MoS_2 (n = 2-6).

Figure S9. Electronic band structure of sh^{n}o-MoS_2 (n = 1-6).

Figure S10. Density of states of sh^{n}o-MoS_2 (n = 1-6).

Figure S11. Band-decomposed charge density of sh^{n}o-MoS_2 (n = 1-5).

Supplementary Tables

Table S1. Structural parameters and band gap of sho-TMD.

Table S2. Structural parameters, total energy, and band gap of sh^{n}o-MoS_2 (n = 1-6).

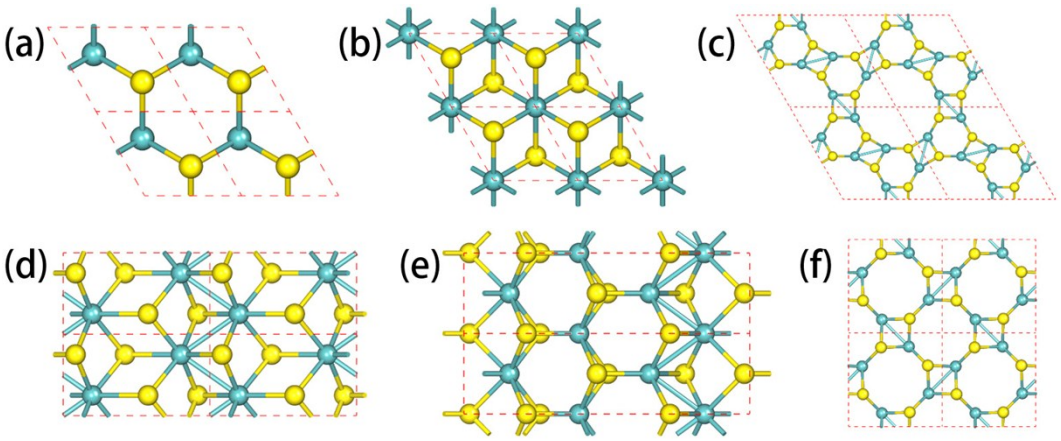

Figure S1. Optimized structures of (a) H-MoS_2, (b) 1T-MoS_2, (c) H′-MoS_2, (d) 1T′-MoS_2, (e) T′′-MoS_2 and (f) so-MoS_2.

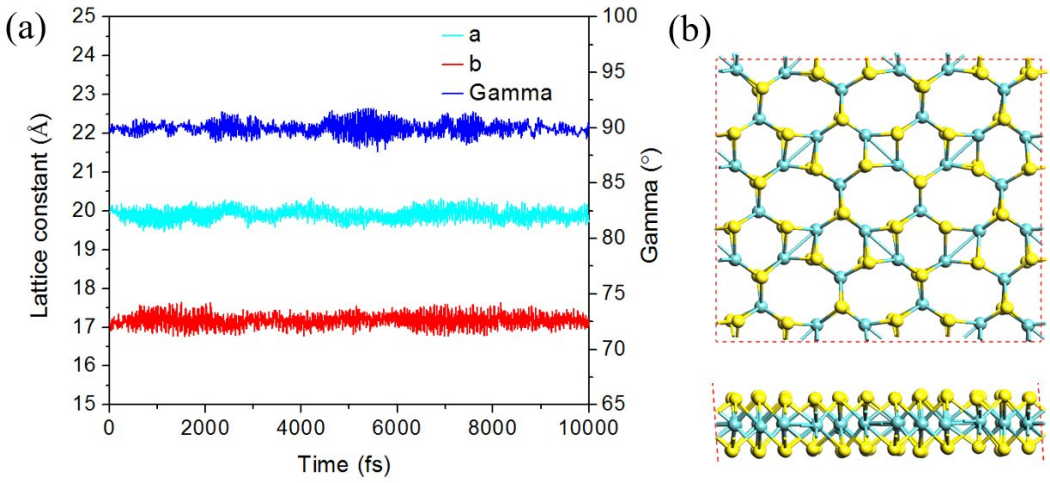

Figure S2. (a) Evolution of lattice parameters a, b, and γ of sho-MoS_2 during the NpT-AIMD simulation at temperature of 300 K. (b) Snapshots of the structure (2×3 supercell) at the end of the simulation.

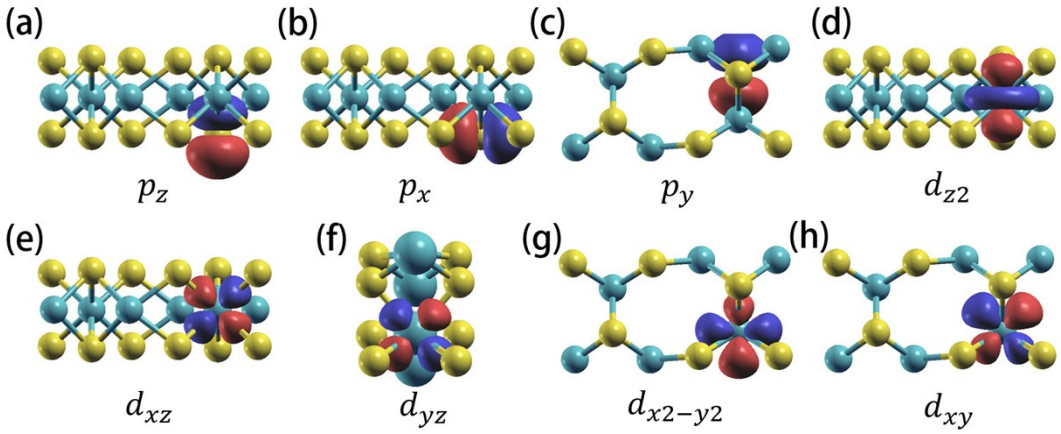

Figure S3. Maximally Localized Wannier functions (MLWFs) of sho-MoS_2, including three S-3p orbitals and five Mo-4d orbitals.

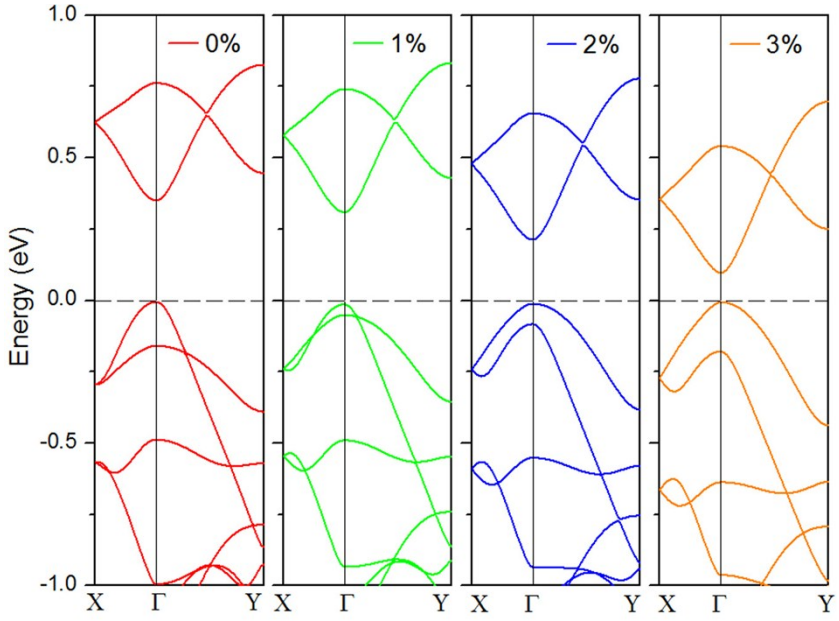

Figure S4. Electronic band structure of sho-MoS_2 under different magnitudes of equi-biaxial tensile strain at the PBE level.

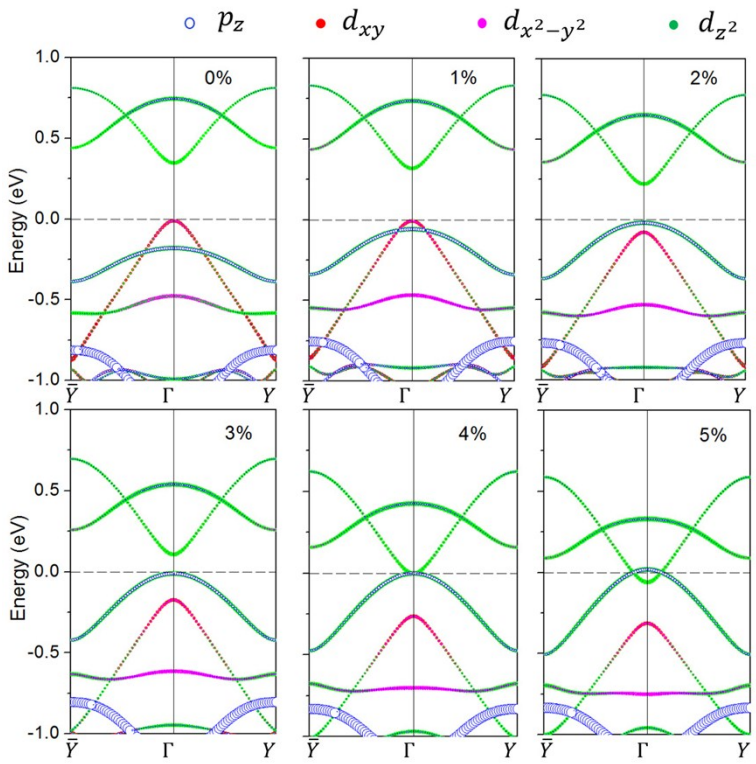

Figure S5. Orbital projected band structure of sho-MoS_2 under different magnitudes of equi-biaxial tensile strains.

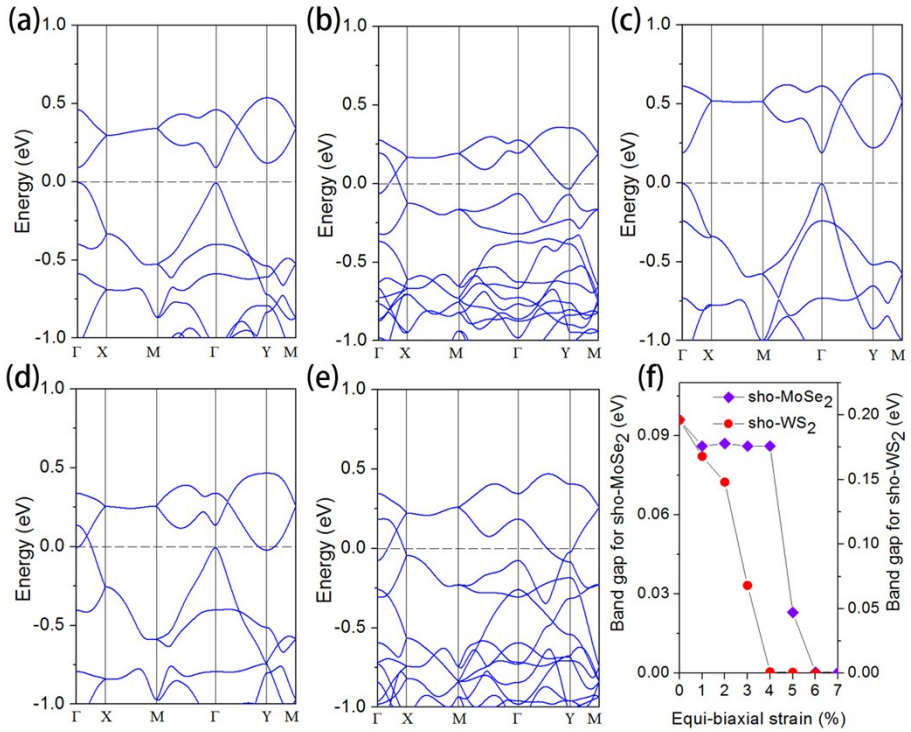

Figure S6. Electronic band structure of (a) sho-$MoSe_2$, (b) sho-$MoTe_2$, (c) sho-WS_2, (d) sho-WSe_2, and (e) sho-WTe_2 calculated using the PBE functional. (f) Energy band

gap as a function of equi-biaxial tensile strain for sho-$MoSe_2$ and sho-WS_2, respectively.

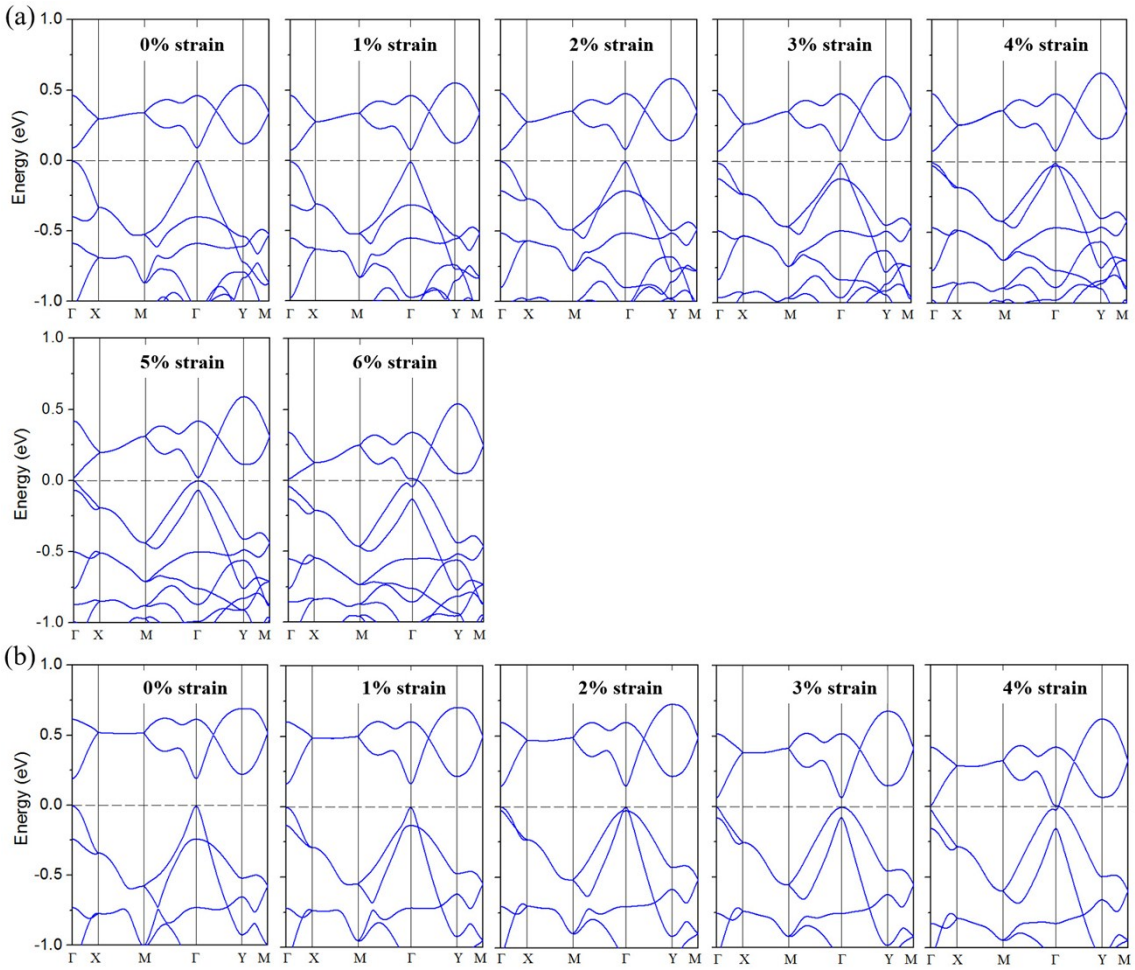

Figure S7. Electronic band structure of (a) sho-$MoSe_2$ and (b) sho-WS_2 under different magnitudes of equi-biaxial tensile strain (at the PBE level).

Table S1. Optimized lattice parameters and electronic band gaps E_g at the PBE level for sho-MX_2 structures, where M = Mo and W, and X = S, Se and Te.

sho-MX_2	a (Å)	b (Å)	E_g (eV)
MoS_2	9.98	5.70	0.35
$MoSe_2$	10.41	5.92	0.10
$MoTe_2$	11.12	6.18	metallic
WS_2	10.02	5.73	0.20
WSe_2	10.42	5.92	metallic
WTe_2	11.08	6.18	metallic

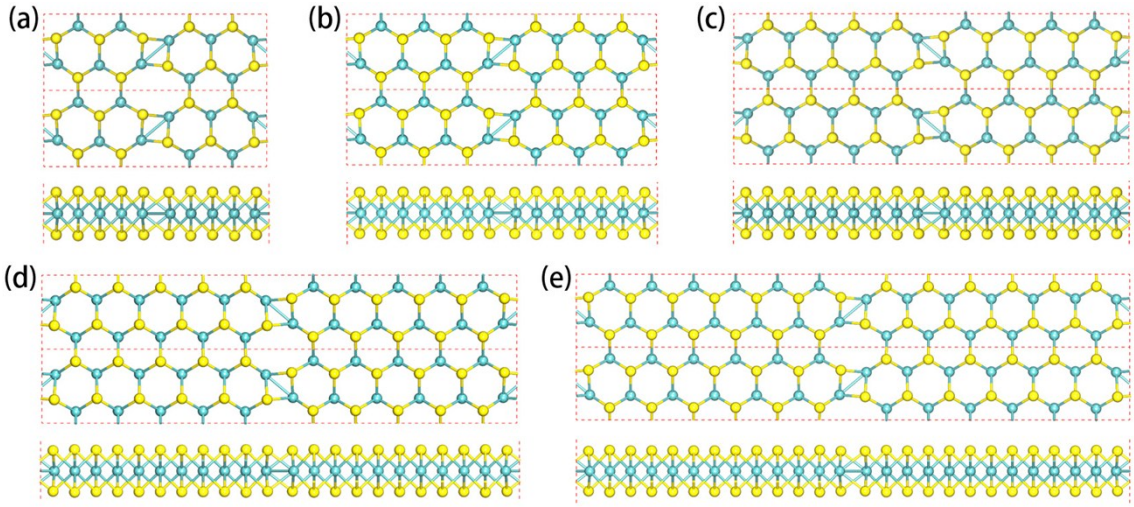

Figure S8. Optimized structures of (a) sh^{2}o-MoS_2, (b) sh^{3}o-MoS_2, (c) sh^{4}o-MoS_2, (d) sh^{5}o-MoS_2, and (e) sh^{6}o-MoS_2 from the top and side views.

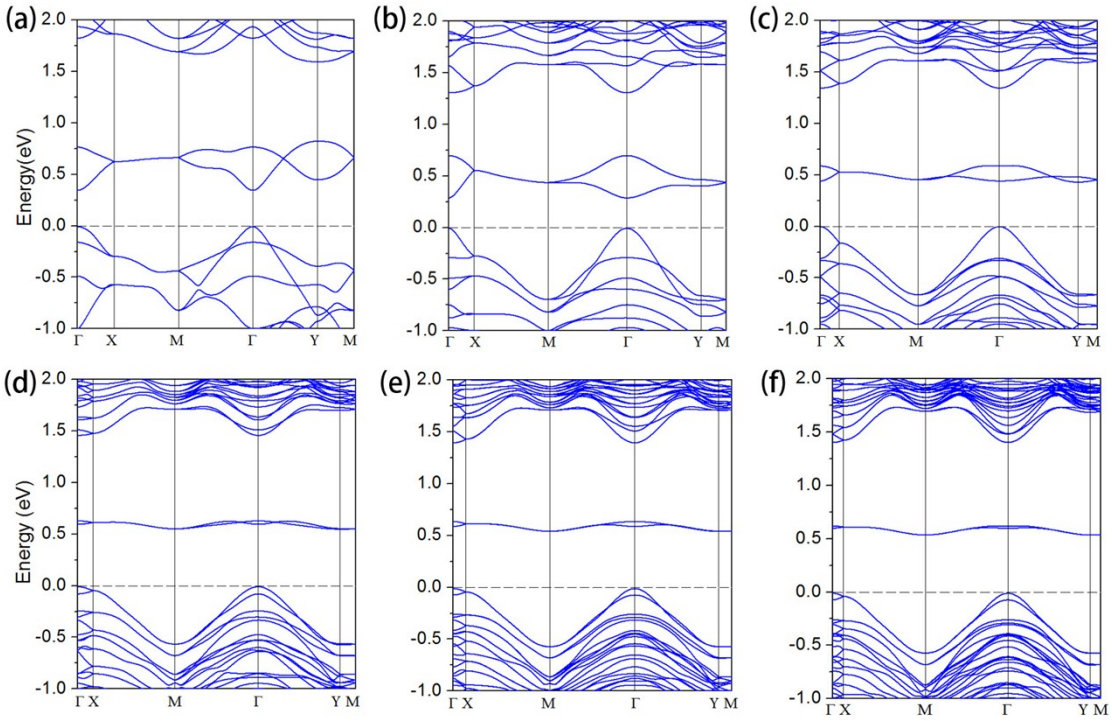

Figure S9. Electronic band structure of (a) sho-MoS_2, (b) sh^2o-MoS_2, (c) sh^3o-MoS_2, (d) sh^4o-MoS_2, (e) sh^5o-MoS_2, and (f) sh^6o-MoS_2 at the PBE level.

From the results in Table S2, one can see that the band gaps of sh^no-MoS_2 structures increase as the value of n increases except for the case of n = 1. This can be attributed to the structure uniqueness of sho-MoS_2. It is found that the charge is mainly distributed in the octagon rings by calculating band-decomposed charge density corresponding to the two lowest unoccupied bands of sh^no-MoS_2. For sh^no-MoS_2 with n value larger than 1, where the neighboring octagons are separated by hexagons along the crystal axis a, so that suppressing the interaction of localized charge in two neighboring octagons. However, for sho-structure, there is no hexagon unit between the neighboring octagonal rings along the crystal axis a, thus the charge localized in the neighboring octagons can directly interact with each other, resulting in the abnormal value of band gap.

Table S2. Optimized lattice parameters, relative energy (E) calculated with respect to H-MoS_2, and band gap (E_g, calculated by using the PBE functional) for sh^{n}o-MoS_2 (n=1-6).

n in sh^{n}o-MoS_2	a (Å)	b (Å)	E (eV/f.u.)	E_g (eV)
1	9.98	5.70	0.60	0.35
2	16.40	5.60	0.37	0.29
3	22.80	5.56	0.27	0.43
4	29.18	5.55	0.21	0.56
5	35.54	5.54	0.17	0.55
6	41.91	5.54	0.15	0.55

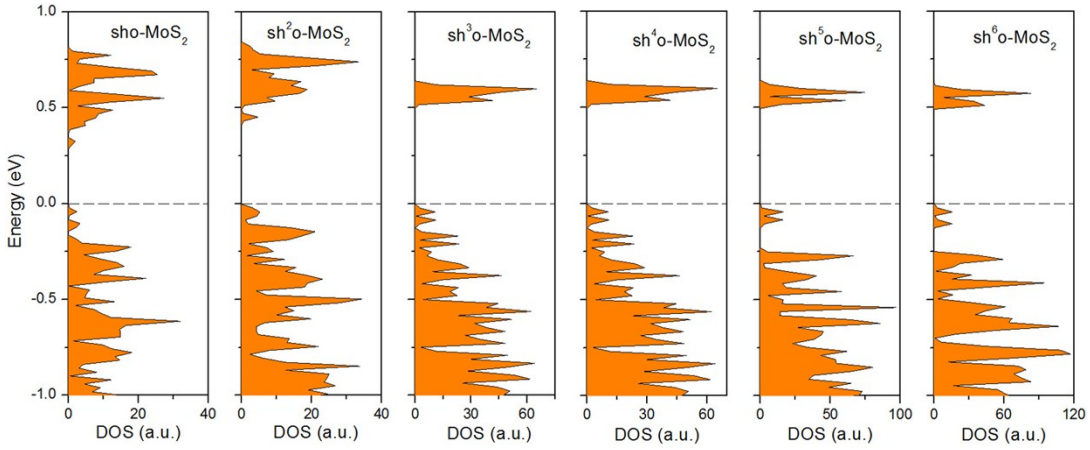

Figure S10. Electronic density of states (DOS) of sho-, sh^{2}o-, sh^{3}o-, sh^{4}o-, sh^{5}o-, and sh^{6}o-MoS_2. Here a.u. represents arbitrary unit.

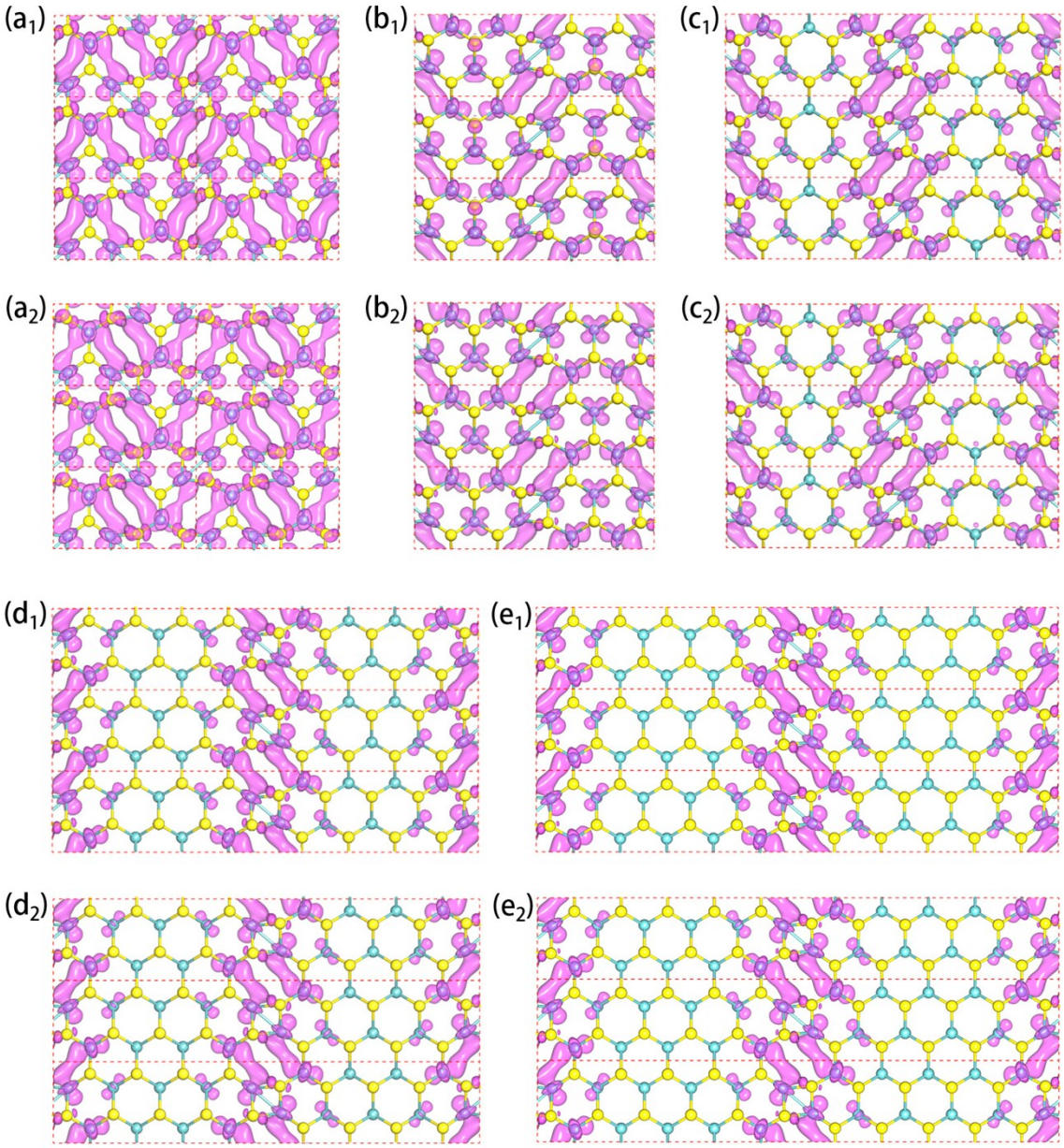

Figure S11. Band-decomposed charge density isosurfaces (isovalue: 0.01 e/Å^3) corresponding to the lowest and the second lowest unoccupied energy bands of sh^{n}o-MoS_2: (a_1) and (a_2) for sho-MoS_2; (b_1) and (b_2) for sh^{2}o-MoS_2; (c_1) and (c_2) for sh^{3}o-MoS_2; (d_1) and (d_2) for sh^{4}o-MoS_2; (e_1) and (e_2) for sh^{5}o-MoS_2. The top and bottom panels are the charge of the lowest and second lowest unoccupied bands, respectively.